ON THE STRUCTURE OF TURBULENCE FIELDS IN A SEPARATED FLOW AROUND A FINITE WING; ANALYSIS USING DIRECT NUMERICAL SIMULATION

Juan Carlos Bilbao-Ludena, George Papadakis
Department of Aeronautics
Imperial College London
Exhibition Rd, South Kensington, London SW7 2BX
jcb4717@ic.ac.uk, g.papadakis@imperial.ac.uk

ABSTRACT

We investigate the spatial distribution and production mechanisms of turbulent kinetic energy around a NACA 0018 wing with square wingtip profile at $Re_c = 10^4$ and 10° angle of attack with the aid of Direct Numerical Simulation (DNS). The analysis focuses on the highly inhomogeneous region around the tip and the near wake; this region is highly convoluted, strongly three-dimensional and far from being self-similar. The flow separates close to the leading edge creating a large, open, recirculation zone around the central part of the wing. In the proximity of the tip, the flow remains attached but another smaller recirculation zone forms closer to the trailing edge; this zone strongly affects the development of main wing tip vortex. We find that the three-dimensional flow separation at the sharp tip close to the leading edge plays an important role on subsequent vortical flow development on the suction side. The production of turbulent kinetic energy and Reynolds stresses is also investigated and discussed in conjunction with the identified vortex patterns with a special focus on the role of vortex stretching/compression. The detailed analysis of the mechanisms that sustain turbulent kinetic energy improves our understanding of these highly three dimensional, non-equilibrium flows and can lead to better actuation methods to manipulate these flows.

INTRODUCTION

The flow physics of the near wingtip field is known to be extremely complex due to its highly turbulent and three-dimensional nature comprising multiple cross-flows. More specifically, wingtip flows involve roll-up of vortex sheets, shear layer instabilities, and boundary layer separation (Green (2012)). It is known that traditional turbulence models that employ the eddy-viscosity concept, cannot capture the effect of rotation (and the associated misalignment between the stress and stain-rate tensors) that characterize vortical flows, and this has led to over-predictions of turbulence production in flows involving round tip profiles (Churchfield & Blaisdell (2009)).

Recent works have investigated the three-dimensional flow around low-aspect-ratio finite wings at low Reynolds number (laminar flow) (Taira & Colonius (2009*a*,*b*); Zhang *et al.* (2020*b*)), focusing mainly on post-stall conditions and the effect of different sweep angles (Zhang *et al.* (2020*a*)). High-fidelity simulations at higher Reynolds numbers in the presence of turbulence have been made (Uzun & Hussaini (2010); Garmann & Visbal (2017); Jiang *et al.* (2008)). In these simulations, shear layers and separated boundary layers have been reported as the leading sources of turbulence in the tip-flow (Jiang *et al.* (2008)). The study of Garmann & Visbal (2017) reports both instantaneous and time-average flows, and shows that the formation, separation, and entrainment of shear-layer substructures within the tip vortex feeding sheet are stationary whereas interactions with the wake are unsteady. Smith & Ventikos (2021) conducted a DNS study, and presented details related to the roll-up process and the behavior of mean axial velocity and mean pressure profiles at relatively low angles of attack.

Despite the recent progress in the fundamental understanding of the general flow features, there is relatively little discussion in the interaction of vortical structures with the developed turbulence field. The main goal of this work is therefore to conduct a thorough analysis of the turbulence production mechanisms in the very near-field of a squared-tip finite wing, including regions far from self-similarity; these are seldom examined and analytical approaches do not apply. In comparison to some of the aforementioned studies, in this work, we aim to study a flow with a multi-scale character and multiple developing secondary flows. This necessitates the use of DNS as a research tool. The revealed magnitudes and location of these mechanisms will lay the foundation for better understanding and modeling/control strategies of these highly non-equilibrium vortical flows.

COMPUTATIONAL DETAILS

In the present work, the flow around a NACA 0018 wing with square wingtip is simulated at a chord-based $Re_c = 10^4$ (value relevant to small and medium-scale unmanned aircrafts) and 10° angle of attack (AoA). The simulation has been performed with the Finite Volume Method (FVM) in-house code PANTARHEI which solves the incompressible Navier-Stokes equations using the fractional step method, with incremental pressure correction to satisfy the continuity equation. The aspect ratio of the wing is equal to 2 and the domain extends one chord length in the spanwise direction beyond the wing tip. The mesh comprises around 63 million cells which are clustered in the vicinity of the airfoil, around the wing tip and the wake. The thickness of the cell closest to the wall has $\Delta y^+ < 0.5$ and the grid spacings in the streamwise and spanwise directions have $\Delta x^+ < 3$ and $\Delta z^+ < 1$ respectively (the plus superscript, $^+$, indicates wall units, as usual). The DNS quality of the mesh was further checked by computing the ra-

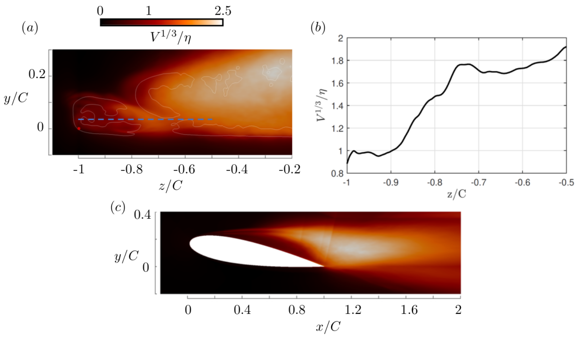

Figure 1. a) Contours of the ratio $V^{1/3}/\eta$ in the $y-z$ plane at $x/C = 1.1$, the location of fully developed turbulence. The white line represents the Q-value (see next section for definition) and the red dot the projected location of the wingtip corner. (b) Plot of $V^{1/3}/\eta$ along the dotted blue line shown in (a) at $y/C = 0.04$. (c) Contour at $x-y$ plane at $z/C = 0.5$ (quarter-span).

tio of the grid size (equal to the cubic root of the cell volume, $V^{1/3}$) to the Kolmogorov length scale, η. Fig. 1(a) shows a contour plot of this ratio in the $z-y$ plane downstream of the trailing edge; the maximum value is below 2.5. In panel (b), the values along the dashed line shown in panel (a) are found to be below 2. Fig. 1(c) shows contours in the $x-y$ plane located at quarter span; again the values do not exceed 2.5.

RESULTS

Main Features of the Near Wake velocity field and vortical structures

Contours of the time-averaged streamwise velocity at different streamwise planes are shown in Fig. 2. The flow separates at $x/C \approx 0.2$ and does not reattach on the suction side of the wing. Close to the leading edge, the separating region occupies most of the span, but once the secondary flow in the wingtip starts to develop, the left boundary is displaced inboard. This creates a recirculating bubble with the outboard end forming an angle with the streamwise direction; this will be seen more clearly in subsequent figures. A 3D separated region with a similar trapezoidal shape has been also observed in Garmann & Visbal (2017) for a wing with a rounded tip profile. It is very interesting to see that at $x/C \approx 0.8$ another small recirculating bubble (indicated by a deep blue color) appears close to the wingtip; this bubble closes in the near wake at $x/C \approx 1.2$. Between the two recirculation regions, a jet with positive velocity appears. As will be seen later, the shear layers in the wall-normal and spanwise directions play a very important role in the turbulence production and distribution of Reynolds stresses across the span. The flow has a wake-like behaviour, i.e $\langle U_1 \rangle < 1$ at all planes (the angular brackets indicate time-averaging). The only region where $\langle U_1 \rangle > 1$ is observed slightly above the wake where the velocity magnitude reaches a value of approximately 1.1.

The Q-criterion was used to identify the emerging coherent structures of the finite wing flow. The identification method λ_2 (Jeong & Hussain (1995)) was also implemented and resulted in similar structures. Q is defined as the second invariant of velocity gradient tensor $\frac{\partial U_i}{\partial x_j}$, i.e. $Q = 0.5\left(\Omega_{ij}\Omega_{ij} - S_{ij}S_{ij}\right)$, where Ω_{ij} and S_{ij} are the components of the instantaneous rotation and strain-rate tensors respectively. Values $Q > 0$ denote a rotation-dominated region, which can be used for vortex identification purposes.

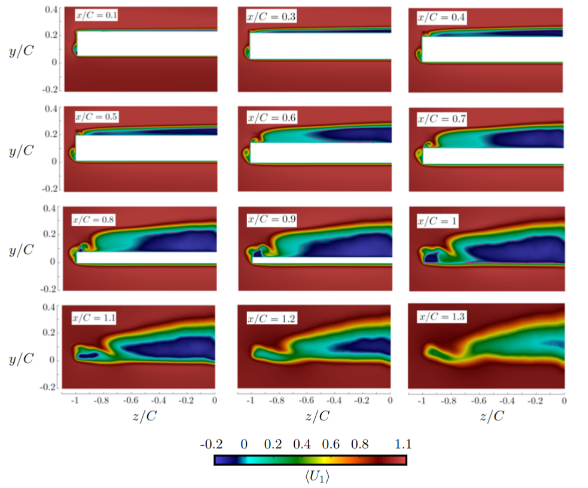

Figure 2. Contours of the mean axial velocity $\langle U_1 \rangle$ at equally spaced planes $x/C = 0.2, ..., 1.3$. The purple-coloured contour line represents $\langle U_1 \rangle = 0$.

Visualization of isosurfaces of the time-average Q-criterion from different viewing angles enables us to understand better the structures that originate in the pressure area and the tip region. Fig. 3 (a) shows clearly one vortex that starts at the flat tip side and grows. This vortex is designated as Left Vortex (LV) and arises due to the spanwise separation of the shear layer emanating from the pressure side of the wing. Near the sharp edge on the suction side, a concentrated vortex starts developing at around $x/C = 0.1$, it grows and subsequently weakens as it approaches the trailing edge; we designate this vortex as V0. The evolution of this vortex can be visualized better in Fig. 3(c); we see that V0 has decayed shortly after the trailing edge. Starting at the same initial plane as V0, the Right Vortex (RV) develops in parallel but its trace is lost at a short distance downstream of the trailing edge. The vortical region $R0$ is defined as the area where the separated shear layers taking part in the roll-up process amalgamate and readjust downstream of the tip. The main trailing vortex V1 originates at $R0$ and persists throughout the computational domain. V2 is another vortex that originates also from R0 but merges further downstream with V1.

The organization of the vortex structure topology at $x/C = 0.75$ is shown in Fig. 3(b) and shows good agreement with visualizations reported in experimental (Katz & Galdo (1989); Bailey *et al.* (2006); Giuni (2013); Birch *et al.* (2003)) as well as computational studies (Smith & Ventikos (2021)) despite employing different Re_c and geometrical setups.

We explore next the origins of the wake tip vortices and their evolution. We consider the streamwise vorticity $\langle \Omega_x \rangle$ and the vorticity intensification $\langle \Omega_j \rangle \langle S_{xj} \rangle$, which can be decomposed into vortex stretching (or axial elongation) and tilting terms,

$$\langle \Omega_j \rangle S_{xj} = \underbrace{\langle \Omega_x \rangle \langle S_{xx} \rangle}_{\text{vortex stretching}} + \underbrace{\langle \Omega_y \rangle \langle S_{xy} \rangle + \langle \Omega_z \rangle \langle S_{xz} \rangle}_{\text{vortex tilting}} . \quad (1)$$

From conservation of angular momentum, a vortex tube undergoing mean stretching, i.e. $\langle S_{xx} \rangle = \frac{\partial \langle U_1 \rangle}{\partial x_1} > 0$, will become more narrow and have increased streamwise vorticity. On the other hand, under mean compression i.e. $\langle S_{xx} \rangle < 0$, the vorticity tube will grow thicker, resulting in a reduced rotational rate (Wu *et al.* (2015)). Fig. 4 presents (filled) contours of

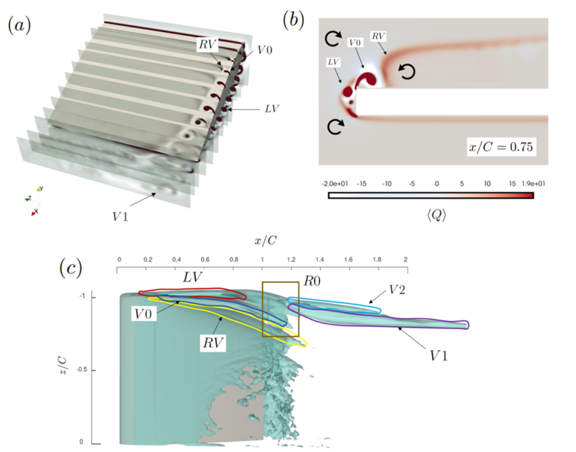

Figure 3. (a) Contours of the time-average $\langle Q\rangle$ at equally spaced planes $x/C = 0.1, 0.2, ..., 1.4$. with designated vortical structures. (b) Organization of the vortex structure topology at $x/C = 0.75$. (c) Visualization and designation of vortical structures using the iso-surface $\langle Q\rangle = 5$.

streamwise strain rate $\langle S_{xx}\rangle$ superposed with isolines of positive vorticity $\langle \Omega_x\rangle$. The arch-like structure that was formed from the secondary flow around the recirculation zone at the tip persists up to about $x/C = 1.1$. This structure carries two regions of concentrated vorticity, located at approximately the same wall normal distance, $y/C = 0.1$, and at spanwise locations $z/C = -1$ and -0.9. The former patch of vorticity quickly disappears, because it is located within a region of compression (dark contours), but the latter patch grows due to stretching (note the yellow-coloured spot of high acceleration at $z/C = 0.9$ in planes $x/C = 0.95 - 1.1$). Eventually this patch will evolve to form the tip vortex V1 that will persist in the wake, see plane $x/C = 1.3$. The core of this vortex is located slightly inboard with respect to the tip, at $z/C \approx -0.9$. This agrees with the theoretical analysis of Milne-Thomson (1973). We conjecture that the high strain rate that leads to the intensification of V1 is due to the recovery of the streamwise velocity downstream of the recirculation bubble that forms around the tip of the trailing edge. It is also interesting to observe that the near wall vorticity patch (that forms between V0 and RV) is immersed in a region of compression shortly downstream of the trailing edge and quickly disappears (it is detected until $x/C \approx 1.1$). Vortex V2 starts to be visible in the lower tip corner in planes $x/C = 0.95 - 1.05$ and undergoes stretching in all planes. It eventually merges with V1, as shown in figure 3(c).

Turbulence structure of the separated wake

In this section, we examine the spatial distribution of turbulent kinetic energy (TKE), k, and its production. The objective is to identify the most intense regions and uncover the main production mechanisms. We focus on the near-field, i.e. distance $5\% - 30\% C$ from the trailing edge. In this region, the flow is far from being self-similar, thus well known viscous vortex models, such as the Burgers or Sullivan vortex (Green (2012); Wu *et al.* (2015)), do not apply.

The increased turbulent activity between the two recirculation bubbles can be detected in the Reynolds stresses isosurface plots shown in Fig. 5. Analysis shows that $\langle u_1u_1\rangle$ and $\langle u_2u_2\rangle$ dominate over $\langle u_3u_3\rangle$. It can be seen that k and $\langle u_1u_1\rangle$ isosurfaces wrap around the outer boundary of V0 and the large bubble originating from the leading edge. The levels of turbulent production and k are small in the V0 core, most likely due to the stabilizing effect of solid body rotation (Zeman (1995)).

We now proceed to study the production terms of the Reynolds stresses of $\langle u_1u_1\rangle$ and $\langle u_2u_2\rangle$, given by Pope (2000),

$$\mathscr{P}_{11}^{R-s} = -2\left[\langle u_1u_1\rangle\frac{\partial\langle U_1\rangle}{\partial x_1} + \langle u_1u_2\rangle\frac{\partial\langle U_1\rangle}{\partial x_2} + \langle u_1u_3\rangle\frac{\partial\langle U_1\rangle}{\partial x_3}\right] \tag{2}$$

$$\mathscr{P}_{22}^{R-s} = -2\left[\langle u_2u_1\rangle\frac{\partial\langle U_2\rangle}{\partial x_1} + \langle u_2u_2\rangle\frac{\partial\langle U_2\rangle}{\partial x_2} + \langle u_2u_3\rangle\frac{\partial\langle U_2\rangle}{\partial x_3}\right] \tag{3}$$

The magnitude of $\langle u_3u_3\rangle$ (and its production) is smaller in comparison with the other two stresses and is not investigated.

Figures 6 and 7 show isosurfaces of $\mathscr{P}_{11}^{R-s}$ and $\mathscr{P}_{22}^{R-s}$ respectively. In each plot, isosurfaces of the most important components that make up the production terms are also plotted. Fig. 6 indicates that the term $-2\langle u_1u_2\rangle\frac{\partial\langle U_1\rangle}{\partial x_2}$ is by far the largest contributor of $\mathscr{P}_{11}$, compare panels (b) and (c). This is of course expected since both the separating shear layer on the suction side and the attached flow in the pressure side are associated with strong shear $\frac{\partial\langle U_1\rangle}{\partial x_2}$ (note however that the production is stronger in the suction side because flow separation results in higher shear). It is also interesting to notice the localised contribution of the normal term, $-2\langle u_1u_1\rangle\frac{\partial\langle U_1\rangle}{\partial x_1}$, which wraps around vortex V0, as can be seen in panel (a).

The production term $\mathscr{P}_{22}^{R-s}$ is shown in panel (b) of Fig. 7. The dominant component is $-2\langle u_2u_2\rangle\frac{\partial\langle U_2\rangle}{\partial x_2}$, which is shown in panel (a). The two other components are not included because their contribution is negligible; this can be attested by the resemblance of the isosurfaces in the two panels. The production term is maximised downstream of the trailing edge, where higher local values of negative normal strain $\frac{\partial\langle U_2\rangle}{\partial x_2}$ are encountered. Assuming that $\frac{\partial\langle U_3\rangle}{\partial x_3}$ is small, from the continuity equation we get $\frac{\partial\langle U_2\rangle}{\partial x_2} = -\frac{\partial\langle U_1\rangle}{\partial x_1}$, so the regions of strong $-2\langle u_2u_2\rangle\frac{\partial\langle U_2\rangle}{\partial x_2}$ are collocated with the areas of rapid streamwise velocity recovery, i.e. large $\frac{\partial\langle U_1\rangle}{\partial x_1}$ acceleration (or normal strain rate). This is the area shortly downstream of the closure of the recirculation region close to the tip.

In order to probe further the interaction between the elongation rate, $\langle S_{xx}\rangle$, vortex stretching, circulation and production of turbulent kinetic energy in the near wake, we integrate the aforementioned quantities in a number of cross-steam planes from $x/C = 1.1 - 2.4$. The boundary of the integration area S_z is shown with a closed dashed line in panels (a) and (b) of Fig. 8, where contours of $-2\langle u_1u_2\rangle\frac{\partial\langle U_1\rangle}{\partial x_2}$ and $-2\langle u_2u_2\rangle\frac{\partial\langle U_2\rangle}{\partial x_2}$ are plotted respectively at plane $x/C = 1.2$. The locations of the planes themselves are marked in Fig. 8(c). The three areas of large production $-2\langle u_1u_2\rangle\frac{\partial\langle U_1\rangle}{\partial x_2}$ in panel (a) correspond to flow originating from the pressure side (bottom horizontal region), the suction side (top right area) and between the two recirculation zones (middle region), see also contours of the total production $P = -\langle u_iu_j\rangle\langle S_{ij}\rangle$ in Fig. 5. The patches of large $-2\langle u_2u_2\rangle\frac{\partial\langle U_2\rangle}{\partial x_2}$ in panel (b) correspond to the two areas shown in Fig. 7(a).

In panel (d) Fig. 8 we plot the variation along x/C of the surface integrals of vortex stretching and axial elongation over S_z. We also superimpose the circulation $\langle \Gamma_x\rangle$ (surface integral

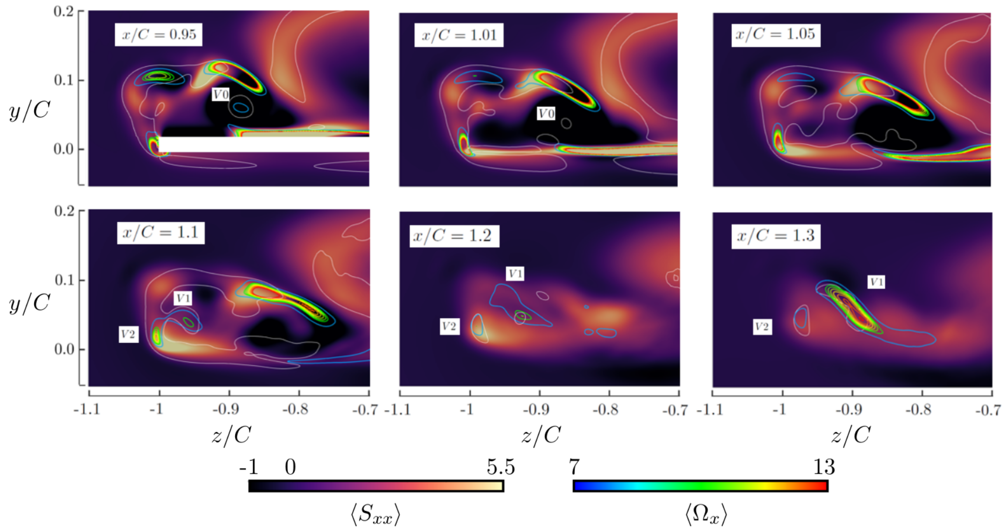

Figure 4. Emergence of the wake tip vortices V1 and V2. Contours of streamwise strain rate $\langle S_{xx}\rangle$ superposed to coloured isolines of positive $\langle \Omega_x \rangle$. The solid white line indicates $\langle Q\rangle = 5$.

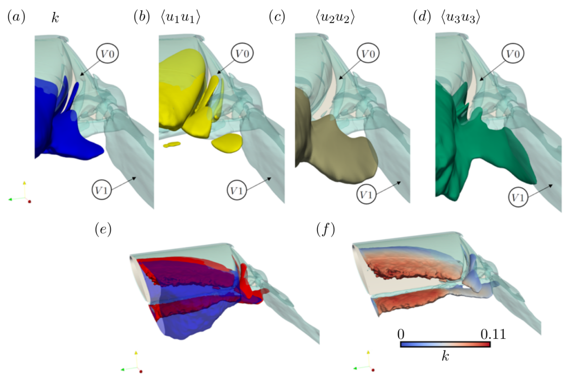

Figure 5. Isosurfaces of (a) k, (b) $\langle u_1u_1\rangle$, (c) $\langle u_2u_2\rangle$ and (d) $\langle u_3u_3\rangle$ at a value of 0.05, 0.05, 0.04 and 0.02 respectively. The contour values correspond to $(a) \approx 45\%$, $(b) \approx 55\%$, $(c) \approx 49\%$,$(d) \approx 29\%$ of their respective positive maximum value at x/C=1.2 in the z-y plane. (e) k - blue contour (0.5) and turbulence production - red contour (0.2). (f) Turbulence production $\mathscr{P}$ colored by k. Hereby, the contour values correspond to $\approx 55\%$ and $\approx 31\%$ of the maximum value of k and $\mathscr{P}$ at x/C=1.2 in the z-y plane. All values are superimposed on $\langle Q\rangle = 5$.

of $\langle\Omega_x\rangle$). This panel shows that the peaks of $\int_{S_z}\langle\Omega_x\rangle\langle S_{xx}\rangle\, dS_z$, $\langle\Gamma_x\rangle$ and $\int_{S_z}\langle S_{xx}\rangle\, dS_z$ are not in phase. The axial elongation term peaks at the streamwise location where $\langle U_1\rangle = 0$ (marked with the vertical dashed line). This is the result of flow recovery, as the flow comes out of the recirculation region around the tip. The vortex stretching term peaks slightly further downstream. The latter term causes the growth of circulation, $\langle\Gamma_x\rangle$ which peaks at about $x/C \approx 1.5$. Note the very weak decay of $\langle\Gamma_x\rangle$ with respect to the other two terms. The only mechanism responsible for the decay for $x/C > 2.0$ is viscous diffusion, which is a slow term and explains the persistence of V1 until the exit of the computational domain. Panel (e) shows that the production component due to shear $-\langle u_1u_2\rangle\frac{\partial\langle U_1\rangle}{\partial x_2}$ peaks earlier compared to the normal component $-2\langle u_2u_2\rangle\frac{\partial\langle U_2\rangle}{\partial x_2}$ and it reaches a higher value. The peak of the former term almost coincides with the location where $\langle U_1\rangle = 0$. Note also the faster decay rate of $-2\langle u_1u_2\rangle\frac{\partial\langle U_1\rangle}{\partial x_2}$ compared to $-2\langle u_2u_2\rangle\frac{\partial\langle U_2\rangle}{\partial x_2}$. While circulation is (almost) constant, both production terms decay because of the solid body rotation velocity profile found in columnar vortices. The fast decay of $-2\langle u_1u_2\rangle\frac{\partial\langle U_1\rangle}{\partial x_2}$ between $x/C \approx 1.2-1.4$ is probably due to the flow recovery away from the recirculation region that smooths the streamwise velocity in the y direction.

CONCLUSIONS

DNS of a half-span NACA 0018 wing with square wingtip profile was performed at a $Re_c = 10^4$ and 10° angle of attack. A thorough analysis of the main vorticity and turbulent production mechanisms above the wing and in the near wake was carried out. The flow was found to separate close to the leading edge and did not reattach on the suction side of the wing. Close to the leading edge, the separating region occupied most of the span, but once the secondary flow in the wingtip started to develop, the left boundary of the recirculating bubble was displaced inboard. In the proximity of the tip, the flow remained attached, but another recirculation zone appeared close to the trailing edge.

The emergence of the main wingtip vortex V1 from the amalgamation and interaction of the different vortices was also elucidated. The presence of the recirculation zone close to the trailing edge resulted in the distortion of the shear layers originating from the pressure side. The distribution of turbulent kinetic energy around the main wing tip vortex V1 was found to be highly asymmetric and high values were concentrated on the right of its axis. Apart from the main separating shear layer, patches of strong production were also found in the area between the two recirculation bubbles in the near wake.

Analysis of the production terms of individual Reynolds stresses has enabled us to uncover the main production mechanisms. It was found that $-2\langle u_1u_2\rangle\frac{\partial\langle U_1\rangle}{\partial x_2}$ is one of the dominant terms responsible for maintaining high levels of $\langle u_1u_1\rangle$. This is the standard production term for wall-bounded flows. Additionally, the wall-normal stress source term $-2\langle u_2u_2\rangle\frac{\partial\langle U_2\rangle}{\partial x_2}$ was responsible for maintaining $\langle u_2u_2\rangle$ primarily in the spiral wakes in the near field.

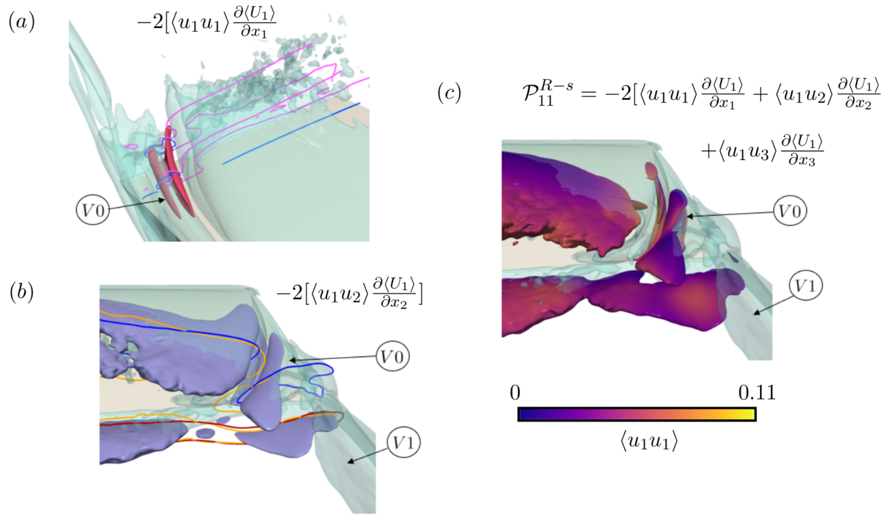

Figure 6. Production terms of $\langle u_1u_1\rangle$ (a) The magenta iso-surface represents $-2[\langle u_1u_1\rangle\frac{\partial\langle U_1\rangle}{\partial x_1}]=0.4$ with pink lines representing the contours of $\langle u_1u_1\rangle=0.03$ and blue line representing compression $\frac{\partial\langle U_1\rangle}{\partial x_1}=-2$. (b) The purple iso-surface represents $-2[\langle u_1u_2\rangle\frac{\partial\langle U_1\rangle}{\partial x_2}]=0.5$, blue lines represents the contours of shear strain coming from the top wing surface with $\frac{\partial\langle U_1\rangle}{\partial x_2}=-7$ and orange lines $\langle u_1u_2\rangle=0.01$, the red line represents shear from the bottom wing surface with $\frac{\partial\langle U_1\rangle}{\partial x_2}=7$ and the corresponding orange line $\langle u_1u_2\rangle=-0.01$ and (d) total production of $\langle u_1u_1\rangle$: iso-surface $\mathscr{P}_{11}^{R-s}=0.3$ colored by $\langle u_1u_1\rangle$. Hereby, the contour values correspond to $(a)\approx 45\%$, $(b)\approx 36\%$ and $(c)\approx 27\%$ of their respective positive maximum value at $x/C=1.2$ (at $x/C=0.9$ for (a)) in the z-y plane. All values are superimposed on $\langle Q\rangle=5$.

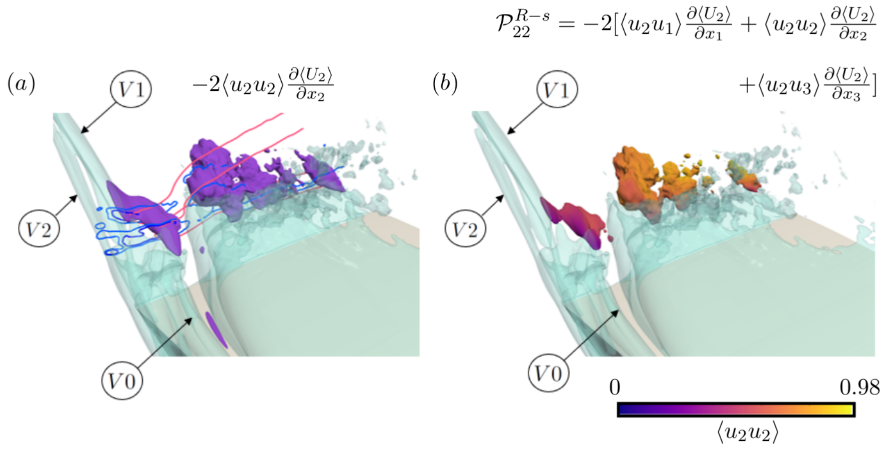

Figure 7. Production terms of $\langle u_2u_2\rangle$ (a) isosurface of $-2\langle u_2u_2\rangle\frac{\partial\langle U_2\rangle}{\partial x_2}=0.3$, blue lines represent contours $\frac{\partial\langle U_2\rangle}{\partial x_2}=-3,-4$ and pink line represents $\langle u_2u_2\rangle=0.04$ (b) isosurface of $\mathscr{P}_{22}^{R-s}=0.3$ colored by $\langle u_1u_1\rangle$. The contour values correspond to $(a)\approx 61\%$ and $(b)\approx 64\%$ of their respective positive maximum value at x/C=1.2 in the z-y plane. All values are superimposed on $\langle Q\rangle=5$.

The vortex stretching rate, axial elongation, streamwise vorticity and production terms were integrated over square y-z surfaces surrounding the V1 vortex, and plotted against the streamwise direction x/C. When the stretching rate became negligible, the circulation (integral of streamwise vorticity) reached a peak and then started to decay very slowly, explaining the persistence of V1 until the end of the computational domain. The production terms become negligible at $x/C\approx 2$ as expected, because the velocity profile within the core of V1 (solid body rotation) cannot sustain turbulence. The detailed analysis presented aims to contribute to a better understanding of separated vortical flows and can hopefully lead to actuation strategies to manipulate them. Future work will also include analysis of the statistics of small-scale turbulent fluctuations undergoing large-scale straining due to the strong shear caused by the main wake.

Acknowledgements

The authors are grateful to the ARCHER2 UK National Supercomputing Service (https://www.archer2.ac.uk), with access via the UK Turbulence Consortium (EPSRC grant EP/R029326/1). Additional computational resources were provided by the UK Materials and Molecular Modelling Hub, which is partially funded by EPSRC (EP/P020194/1 and EP/T022213/1) and Imperial College London. The first author would like to acknowledge the financial support by the National Program of Scholarships and Educational Credit (PRONABEC) of Peru as part of the Beca Generación Bicentenario PhD scholarship.

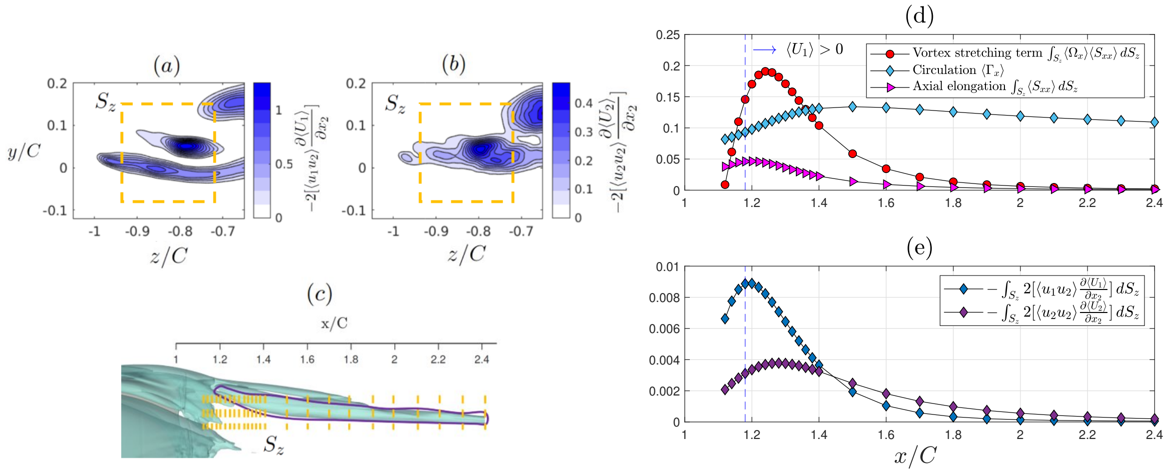

Figure 8. (a) Contours of $-2[\langle u_1 u_2\rangle \frac{\partial\langle U_1\rangle}{\partial x_2}]$ (b) $-2[\langle u_2 u_2\rangle \frac{\partial\langle U_2\rangle}{\partial x_2}]$ superimposed with the integration surface S_z at $x/C = 1.2$. (c) Streamwise locations of the integration surfaces superimposed on $\langle Q\rangle = 5$. Streamwise evolution of quantities related to (d) the vorticity field and (e) the production of Reynolds stresses. The quantities shown are integrated over the surface S_z marked in panels (a) and (b). The vertical dashed line indicates the streamwise location where $\langle U_1\rangle = 0$.

REFERENCES

Bailey, SCC, Tavoularis, S & Lee, BHK 2006 Effects of free-stream turbulence on wing-tip vortex formation and near field. *Journal of aircraft* **43** (5), 1282–1291.

Birch, D, Lee, T, Mokhtarian, F & Kafyeke, F 2003 Rollup and near-field behavior of a tip vortex. *Journal of Aircraft* **40** (3), 603–607.

Churchfield, Matthew J & Blaisdell, Gregory A 2009 Numerical simulations of a wingtip vortex in the near field. *Journal of Aircraft* **46** (1), 230–243.

Garmann, Daniel J & Visbal, Miguel R 2017 Investigation of the unsteady tip vortex structure on a naca0012 wing at fixed incidence. In *55th AIAA Aerospace Sciences Meeting, AIAA SciTech Forum,(AIAA 2017-1002)*.

Giuni, Michea 2013 Formation and early development of wingtip vortices. PhD thesis, University of Glasgow.

Green, Sheldon 2012 *Fluid vortices*, , vol. 30. Springer Science & Business Media.

Jeong, Jinhee & Hussain, Fazle 1995 On the identification of a vortex. *Journal of fluid mechanics* **285**, 69–94.

Jiang, Li, Cai, Jiangang & Liu, Chaoqun 2008 Large-eddy simulation of wing tip vortex in the near field. *International Journal of Computational Fluid Dynamics* **22** (5), 289–330.

Katz, J & Galdo, J Bueno 1989 Effect of roughness on rollup of tip vortices on a rectangular hydrofoil. *Journal of Aircraft* **26** (3), 247–253.

Milne-Thomson, Louis Melville 1973 *Theoretical aerodynamics*. Courier Corporation.

Pope, Stephen B 2000 *Turbulent flows*. Cambridge university press.

Smith, TA & Ventikos, Y 2021 Wing-tip vortex dynamics at moderate reynolds numbers. *Physics of Fluids* **33** (3), 035111.

Taira, Kunihiko & Colonius, Tim 2009*a* Effect of tip vortices in low-reynolds-number poststall flow control. *AIAA journal* **47** (3), 749–756.

Taira, Kunihiko & Colonius, TIM 2009*b* Three-dimensional flows around low-aspect-ratio flat-plate wings at low reynolds numbers. *Journal of Fluid Mechanics* **623**, 187–207.

Uzun, Ali & Hussaini, M Yousuff 2010 Simulations of vortex formation around a blunt wing tip. *AIAA journal* **48** (6), 1221–1234.

Wu, Jie-Zhi, Ma, Hui-Yang & Zhou, Ming-De 2015 *Vortical flows*, , vol. 28. Springer.

Zeman, O 1995 The persistence of trailing vortices: a modeling study. *Physics of Fluids* **7** (1), 135–143.

Zhang, Kai, Hayostek, Shelby, Amitay, Michael, Burtsev, Anton, Theofilis, Vassilios & Taira, Kunihiko 2020*a* Laminar separated flows over finite-aspect-ratio swept wings. *Journal of Fluid Mechanics* **905**.

Zhang, Kai, Hayostek, Shelby, Amitay, Michael, He, Wei, Theofilis, Vassilios & Taira, Kunihiko 2020*b* On the formation of three-dimensional separated flows over wings under tip effects. *Journal of Fluid Mechanics* **895**.